



A novel finite element investigation of cutting force in orthogonal cutting considering plough mechanism with rounded edge tool

Weiwei Zhang¹ · Kejia Zhuang¹ · Donglin Pu^{2,3}

Received: 12 January 2020 / Accepted: 25 May 2020 / Published online: 19 June 2020
© Springer-Verlag London Ltd., part of Springer Nature 2020

Abstract

The plough phenomenon generated by the micro-scale cutting edge plays an important role in tool wear, chip formation and surface integrity. In this study, the plough mechanism in orthogonal cutting with rounded edge tool is investigated by finite element method (FEM). The separation line is developed to determine the contact behavior between rounded edge tool and workpiece. Especially, the workpiece material flow is explored in detail with the definition of separation line. Three contact regions are identified and three frictional force components along the cutting edge are proposed. Then, the Johnson-Cook constitutive model and Johnson-Cook ductile damage criteria are used to describe the plastic deformation and damage mechanics in the cutting simulation with ABAQUS. A developed method based on finite element analysis is proposed to identify three force components individually, including separation line determination based on nodal displacement and three contact region determination with partition function. The accuracy and correctness of the novel FEM model are validated by a series of orthogonal cutting processes. Moreover, the nonlinearly increase relationship between specific cutting energy and edge radius is discussed considering size effect.

Keyword Plough mechanism · Rounded edge tool · FEM · Size effect

1 Introduction

In the cutting process, cutting conditions and cutting parameters need to be adjusted to avoid overload of forces for surface quality and productivity requirements [1]. Furthermore, predicting cutting forces is available in calculating power requirements and selecting geometrical structure. Micro-scale geometry of tool affects the surface integrity, tool wear and temperature distribution significantly. In recent years, cutting tool with round edge, where impact resistance and tool tip strength are increased largely [2], has been widely used in high-precise cutting. In cutting with rounded edge tool,

round edge radius and uncut chip thickness (UCT) are always at the same level. Thus, plough mechanism, which is associated with sliding and intending action [3], always plays an important role and needs to research in detail.

Plough mechanism is first proposed by Albrecht [4] who thought the pressure occurring along the round edge is different from the pressure in cutting tool's face, based on the fact that the cutting edge is not completely sharp. After then, many researchers explored the plough theory in some different situations. Basuray et al. [5] studied plough mechanism based on the chip formation analysis; he pointed out that there must be one critical line to separate chip formation and machined surface formation. Waldorf et al. [3] developed a slip line theory to describe plough mechanism in orthogonal cutting with an assumption of a stable build-up edge adhered to round edge. The minimum uncut chip thickness (MUCT) is signified to be ubiquitous in micromachining. There is no chip formation with UCT lower than MUCT and this phenomenon actually results from plough mechanism. Liu et al. [6] predicted the value of MUCT using FEM in precision micromachining and researched the relationship between surface integrity and MUCT. Yuan et al. [7] established the explicit analytical expression between MUCT and cutting tool sharpness, including

✉ Kejia Zhuang
zhuangkj@whut.edu.cn

¹ Hubei Digital Manufacturing Key Laboratory, School of Mechanical and Electronic Engineering, Wuhan University of Technology, Wuhan, China

² Wuxi Research Institute of Huazhong University of Science and Technology, Wuxi, China

³ Technology Center, Wuxi Turbine Blade Co., Ltd., Wuxi, China

the friction coefficient effect, while Camara et al. [8] used acoustic emission signals to identify the value of MUCT in micro-milling process. Wan et al. [9] used an analytical way to predict MUCT in micro-milling process with the assumption of dead metal theory. Some researchers concluded that the size effect is because of plough mechanism [10, 11]. In addition, the plough mechanism can also deeply affect cutting tool wear, material flow stress, chip formation and especially machined surface integrity [12]. Plough mechanism leads to various specific phenomena under different conditions and cutting force considering plough mechanism is researched in this study.

Many researchers have explored cutting forces considering plough mechanism in cutting with rounded edge tool. Wyen et al. [13] achieved circle fitting of round edge and explored cutting forces with different edge radius using the experimental method. Armarego et al. [14] used a semi-empirical method to define the cutting force component and edge force component. They noted the former component is proportionate to UCT, while the latter component is induced by plough behavior. Stevenson [15] defined cutting force in zero depth of cut as parasitic force, which is associated with plough mechanism and got the force values through orthogonal cutting without feed motion. Guo et al. [12] thought cutting force with no chip formation should be defined as plough force and used extrapolation method to determine plough force. Weng et al. [16] set up a PSO-based semi-analytical force model based on experimental values to investigate plough force. Popov et al. [17] compared extrapolation method with the comparison method of total cutting forces in identifying plough force. Experimental method exploring plough force may be more credible but difficult and farfetched, relatively. In recent years, many researchers have been using FEM to support the determination of cutting force considering plough mechanism. Gonzalo et al. [18] proposed a FEM model to obtain plough force coefficient for a mechanistic milling model. Jin et al. [19] used a 2D finite element model to predict plough force for milling with Brass 260, where arbitrary Lagrangian-Eulerian (ALE) way was used. Gao et al. [20] expressed plough force as micro-milling force and established a 3D milling finite element model to predict micro-milling force during micro-milling of single-crystal superalloy. Wan et al. [21] simulated the formation of dead metal zone under different round edge radius through ALE way.

In cutting force research, few scholars pay attention to contact behavior. However, it is believed that plough mechanism has an influence on the contact situation in cutting. Woon et al. [22] researched tool-based contact phenomenon considering dead metal zone in micromachining through FEM and distinguished the sticking and sliding region in cutting process. Ulutan et al. [23] set up an analytical contact stress model in tool round edge and meanwhile determined the effect of edge radius on the contact situation in the rake face.

In this research, tool-based cutting forces considering plough mechanism are researched. The determination of contact behavior between round edge and workpiece is based on plough mechanism. The separation line is introduced to identify different contact regions and tool-based cutting force components are proposed accordingly. In terms of implementation methods, a 2D finite element cutting model is built to reveal plough mechanism, including prediction of separation line. Moreover, a complicated method based on partition function in ABAQUS software is developed to distinguish every single proposed force component individually.

This paper consists of six sections. Section 1 mainly introduces the background of plough mechanism and the novelty of this work. In Section 2, three force components are described in detail based on the separation line existing in plough mechanism. The concrete and complex FEM operation is given in Section 3. In this section, the observation of the separation line is presented and identification of force components is achieved through numerical simulation. Experimental validation demonstrated to ensure the accuracy and correctness of finite element model is illustrated in Section 4. The results are given and analyzed in Section 5, composed of exploring size effect with different round edge radius. The conclusions are drawn in Section 6.

2 Theoretical analysis

2.1 Plough process with separation line

In practice, round edge with a radius cannot be unavoidably generated and the tool always has a certain edge radius on which the corresponding force acts [11, 24]. This force can be explained by the plough mechanism. Figure 1 shows the whole plough process [4] in cutting. BMF is a small metal area in front of round edge. It is the plough action by round edge

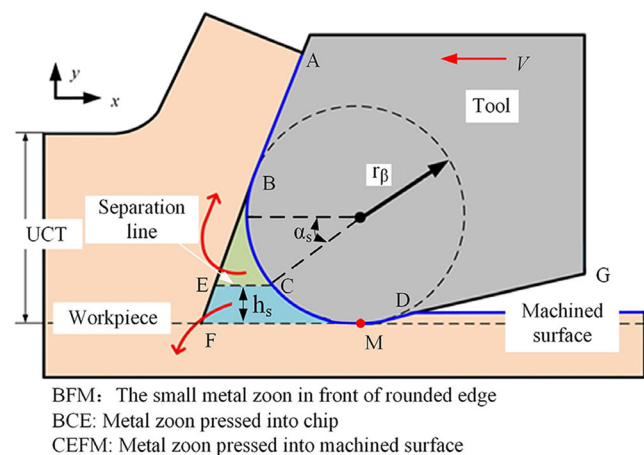


Fig. 1 Material deformation in orthogonal cutting process under rounded edge tool

that results in the deformation of BMF. During the deformation process, the material above CE (BCE in Fig. 1) is pressed into the chip and the rest part (CEFM in Fig. 1) is compressed into machined surface. This complex action reveals plough mechanism and promotes both chip formation and machined surface formation. As the detailed analysis above, there must be one critical dashed line (CE) existing in plough process as shown in Fig. 1.

The material under this line forms the machined surface while the material up this line becomes the chip. Albrecht [4] pointed out that all material above one horizontal dashed line formed the chip and Waldorf et al. [3] summarized the critical rake angle α_s at the separation point C shown in Fig. 1 is around 70° . In machining operation, it is popularly thought that when UCT is lower than this critical line, chip formation will not happen during cutting process. The thickness of this line is defined as MUCT and is of critical to cutting operation.

There are some different descriptions of horizontal dashed line aiming at different situations. This study describes the horizontal dashed line as separation line and the critical thickness is defined as h_s ; the geometrical relationship between edge radius (r_β) and h_s is expressed as Eq. (1).

$$h_s = r_\beta(1 - \cos\alpha_s) \tag{1}$$

2.2 Force components in orthogonal cutting

In Fig. 2, x direction is the main cutting direction and feed direction is along y -axis. Point A represents the point where the chip is separated from the rake face. Points B and D are the end of the rake and clearance roundness, respectively. Point C is an imaginary point on the round edge, which is the intersection of the separation line and the round edge. As shown in Fig. 2, points B and C separate the whole contact zone (AD) into three contact regions. Region c is the contact zone between chip and rake face; region r is the contact zone between chip and round edge, while the contact zone between workpiece and cutting tool is represented as region m.

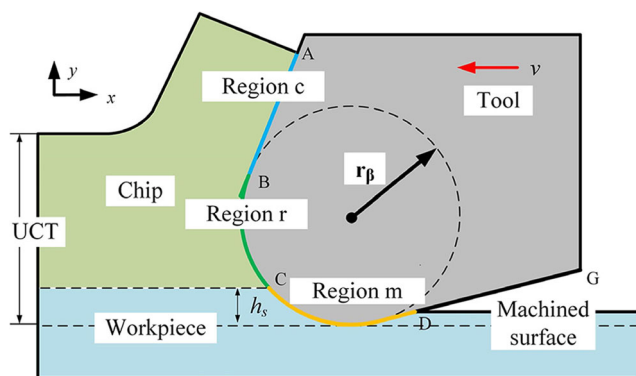


Fig. 2 Force components based on separation line with rounded edge tool in orthogonal cutting process ($i = x, y$)

In the study of the cutting with a complete sharp cutting edge, the contact behavior between round edge and work is always ignored, which is obviously insufficient. This detailed paper analyzes the ploughing process and separation line identifies the contact region along round edge. The proposed three contact region makes it more in-depth and standardized to research contact behavior.

To observe and explore the contact behavior more intuitively, three tool-based contact force components are proposed. As expressed in Eq. (2), F_{ci} , F_{ri} and F_{mi} represent contact force in region c, region r and region m, respectively. In cutting, the whole cutting force (F_i) is the summation of these three force components. The proposal of contact force can simplify the method calculating cutting force and in this study, FEM is used to distinguish three force components. The FEM operation is detailed described in Section 2.

$$F_i = F_{ci} + F_{ri} + F_{mi}(i = x, y) \tag{2}$$

3 Numerical simulation

FEM is used to explore plough process in this study, including plough mechanism verification and contact behavior determination

3.1 Geometrical model

The length and width of the workpiece are reasonably arranged according to the experiment shown in Fig. 3; h is the UCT in the orthogonal cutting. The round edge radius is about $39 \mu\text{m}$ in this study after processing tool passivation, which can improve the processing efficiency largely. The stagnation angle α has been confirmed to vary from 20° to 50° by a wide range of published articles [25]. Therefore, the separation line in this study is

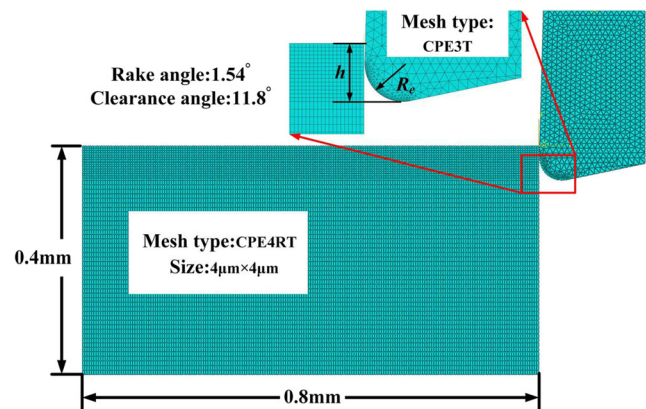


Fig. 3 Geometrical model in orthogonal cutting

estimated to be around 10 μm according to Eq. (1). As a result, to maintain the accuracy and efficiency of the simulation, the size of elements making up the workpiece is 4 μm × 4 μm. The element type of workpiece is CPE4RT, while the tool element type is CPE3T. As for boundary conditions of two-dimensional simulation model, the degrees of workpiece freedom are restricted in all directions, while cutting tool moves in cutting direction with the cutting speed.

3.2 Physical model

Al 7075-T6 and carbide are selected to be the materials of the workpiece and cutting tool. Table 1 shows the material property parameters. Besides, the material constitutive model should be selected properly. From the angle of material deformation, the cutting is special for that workpiece experiences the complete life course of the material including four stages, defined as elastic deformation, plastic deformation, the evolution of damage and material failure. In this study, the Hook law is used to describe the elastic behavior as shown in Eq. (3).

$$\bar{\sigma} = K \cdot \bar{\varepsilon} \tag{3}$$

where $\bar{\sigma}$ and $\bar{\varepsilon}$ denote the equivalent flow stress and strain respectively, and K represents Young’s modulus.

The Johnson-Cook constitutive model is used to define the plastic process in this study. As expressed in Eq. (4), the effect of strain, strain rate and temperature is described in this model by three multiplication components on the right side of the formula respectively. Table 2 shows material constants to describe this model. *A*, *B*, *C*, *n* and *m* represent the initial yield stress, strength coefficient, strain-rate dependency coefficient, strain work-hardening exponent and thermal softening exponent, respectively. It should be noted that all these five material constants can be obtained by torsion tests [26]. Besides, $\bar{\varepsilon}^{pl}$, $\dot{\bar{\varepsilon}}^{pl}$ and ε_0 are equivalent plastic strain, equivalent plastic strain rate and the reference plastic strain rate,

Table 1 The material property parameters in simulation

Material	Al 7075-T6	Carbide
Density (ton/mm ³)	2.81e−9	15e−9
Specific heat (mJ/ton·°C)	0.96e9	0.203e9
Coefficient Of Thermal expansion (°C ^{−1})	23.6e−6	4.7e−6
Young’s Modulus (MPa)	71,700	800,000
Thermal conductivity (w/m·°C)	173	46
Poisson’s ratio	0.33	0.2
Room temperature(°C)	20	20

Table 2 The parameters of Al 7075-T6 for J-C constitutive model [27]

Material	<i>A</i> (MPa)	<i>B</i> (MPa)	<i>C</i>	<i>n</i>	<i>m</i>
Al7075-T6	546	678	0.024	0.71	1.56

respectively. *T*, *T_m* and *T_r* are current temperature, room temperature and melting temperature, respectively.

$$\bar{\sigma} = \left[A + B \left(\frac{\bar{\varepsilon}^{pl}}{\varepsilon_0} \right)^n \right] \cdot \left[1 + C \ln \left(\frac{\dot{\bar{\varepsilon}}^{pl}}{\varepsilon_0} \right) \right] \cdot \left[1 - \left(\frac{T - T_r}{T_m - T_r} \right)^m \right] \tag{4}$$

The J-C ductile damage criteria expressed in Eq. (5) is used to describe the damage initiation. In this model, *d1*~*d5* are material failure constants shown in Table 3; $\bar{\varepsilon}_D^{pl}$, σ_p and σ_{mis} are equivalent plastic strain at the onset of damage, hydrostatic pressure and the von Mises equivalent stress, respectively [28].

$$\bar{\varepsilon}_D^{pl} = \left[d_1 + d_2 \exp \left(-d_3 \frac{\sigma_p}{\sigma_{Mises}} \right) \right] \cdot \left[1 + d_4 \ln \left(\frac{\dot{\bar{\varepsilon}}^{pl}}{\varepsilon_0} \right) \right] \cdot \left(1 + d_5 \frac{T - T_r}{T_m - T_r} \right) \tag{5}$$

Equation (6) defines the effective plastic displacement (\bar{u}^{pl}) using the characteristic length of the element (*L*).

$$\bar{u}^{pl} = L \cdot \bar{\varepsilon}^{pl} \tag{6}$$

In this study, the damage evolution is represented by the variable with the relative plastic displacement *D* [29]. The expression of damage evolution follows as Eq. (7).

$$D = \frac{\bar{u}^{pl}}{\bar{u}_f^{pl}} \tag{7}$$

where \bar{u}_f^{pl} is the effective plastic displacement when material failure happens.

The meshed part is deleted from the simulation when material stiffness is fully degraded [29]. The stiffness state is calculated using the parameter *D* in Eq. (7), when *D* = 0, the material holds nondestructive stiffness; *D* = 1 stands for the

Table 3 The constant parameters of Al 7075-T6 for J-C failure model [27]

Material	<i>d</i> ₁	<i>d</i> ₂	<i>d</i> ₃	<i>d</i> ₄	<i>d</i> ₅
Al 7075-T6	− 0.068	0.451	− 0.952	0.036	0.697

Fig. 4 Nodal displacement by simulation with rounded edge

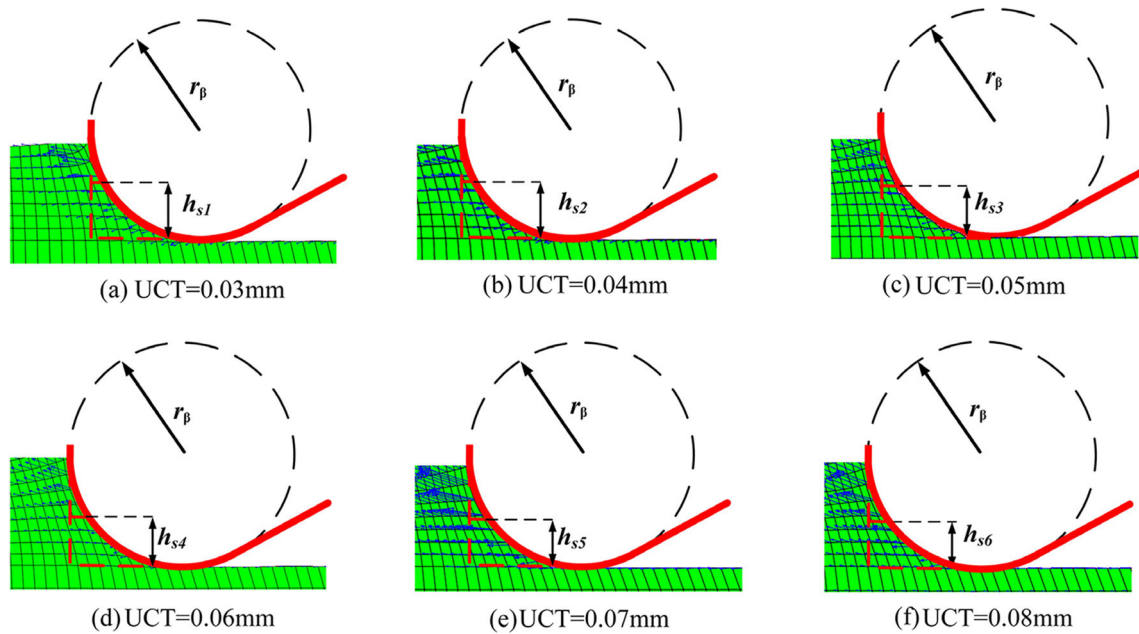
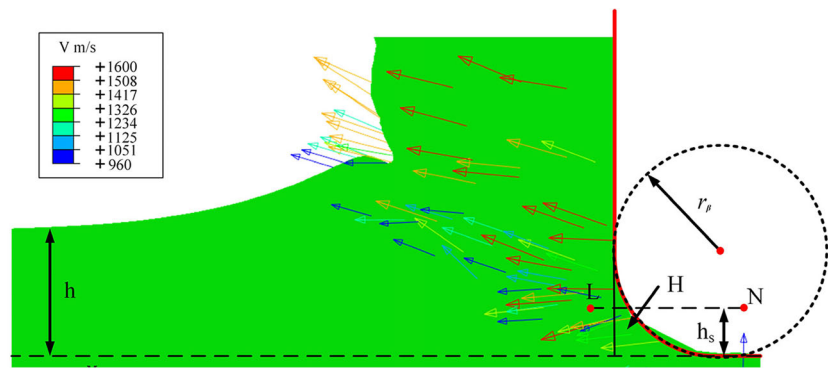


Fig. 5 Nodal displacement in different UCT

complete material stiffness failure, and meanwhile the failed meshed part is removed.

3.3 Material separation and nodal displacement

A series of simulations have been worked to observe the material separation in orthogonal cutting with the cutting speed is 1600 mm/s. Figure 4 shows the nodal displacement obtained from software ABAQUS, which can be used to illustrate the material deformation. The edge radius is set as 0.039 mm and the depth of cut (h) is set as 0.04 mm. The arrows in Fig. 4

show the direction of material flow. As shown in zone H, there is a distinct separation line LN, up which the vertical component of arrows is in the direction of leaving the workpiece, and arrows below this critical line approach the workpiece.

To make results more convincing and accurate, Fig. 5(a)–(e) illustrates the material deformation with UCT = 0.03 to 0.08 mm, respectively. The values of h_s with various UCT are given in Table 4. All values are around 0.015 mm in spite of a little reduction with UCT increasing and thus the value of h_s is decided to be 0.015 mm. However, it should be noted the size of the element is $4 \mu\text{m} \times 4 \mu\text{m}$ with

Table 4 The value of h_s with different UCT. ($r_\beta = 0.039$ mm)

	(a)	(b)	(c)	(d)	(e)	(f)
h/mm	0.03	0.04	0.05	0.06	0.07	0.08
h_s/mm	0.013–0.017	0.013–0.017	0.015	0.015	0.013–0.016	0.012–0.015

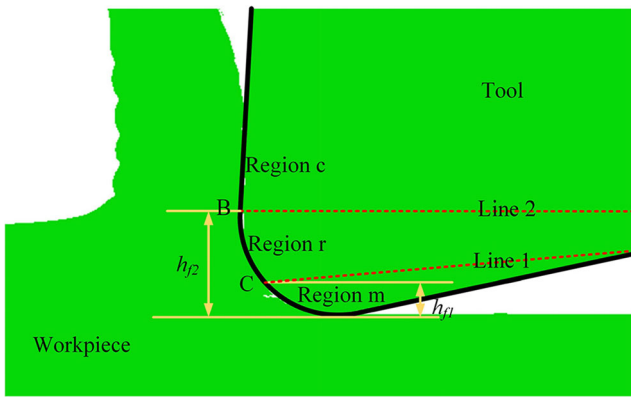


Fig. 6 The partition of cutting tool in software ABAQUS

consideration of simulation efficiency, resulting in the inherent error in the determination of critical value of h_s in this work.

3.4 Identification of force components

In this study, two fictitious lines (line 1, line 2) are assumed to separate the cutting tool as shown in Fig. 6. Point C represents the separation point and the value of h_{j1} is the same as h_s . Point B is the end of rake roundness; h_{j2} represents the vertical distance between the machined face and the end of rake roundness. The separation in Fig. 6 is achieved through the partition function in ABAQUS software. As a result, the whole cutting edge is divided into three regions. In finite element analysis, the cutting edge consists of lots of nodes after meshing and contact force of every single node can be achieved in simulation. Therefore, contact forces in a specific contact region can be calculated from sum of nodal contact force. As expressed in Eq. (8), FN_{jik} and FS_{jik} are the CNORMF (normal component of nodal contact force) and CSHEARF (frictional shear component of nodal contact force) of the node k , respectively. The whole contact force in a cutting region is expressed as F_{ji} . Figure 7 shows the value of forces with the cutting conditions $h = 0.05$ mm, $v = 1600$

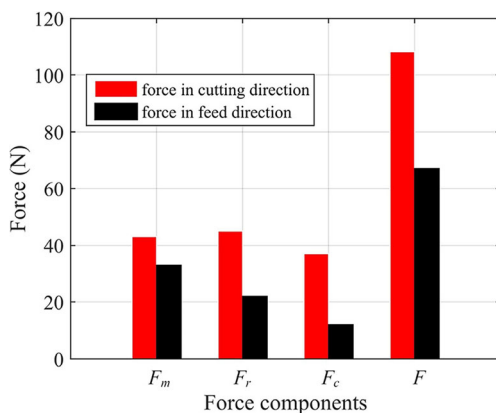


Fig. 7 Identifying force components by simulation

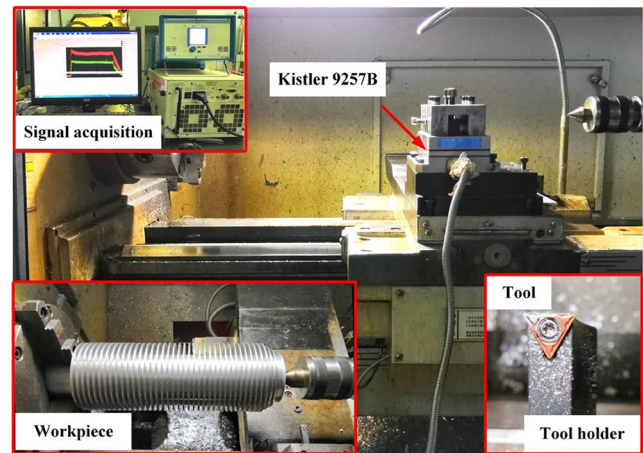


Fig. 8 Orthogonal cutting experiment setup

mm/s and the width is 2 mm. It offers that three contact force components are distinguished successfully by the proposed method, verifying the feasibility of this finite element method.

$$F_{ji} = \sum_{k=1}^n (F_{jik}^S + F_{jik}^N) \tag{8}$$

where j represents m, r, c ; k is the number of nodes distributing along the cutting edge.

4 Experimental validation

In this section, orthogonal cutting experiments are established to validate the accuracy of the cutting forces achieved by FEM.

The experiment set up is shown in Fig. 8. Orthogonal cutting experiments are achieved on a rigid, high precision lathe, which type is CAK5085nzj. Figure 9 shows the geometrical structure of the rounded edge tool used in the experiment. The radius of cutting tool is approximately $39 \mu\text{m}$ measured by

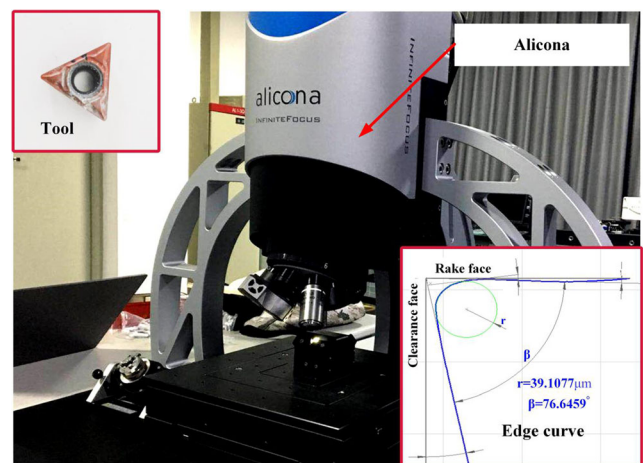
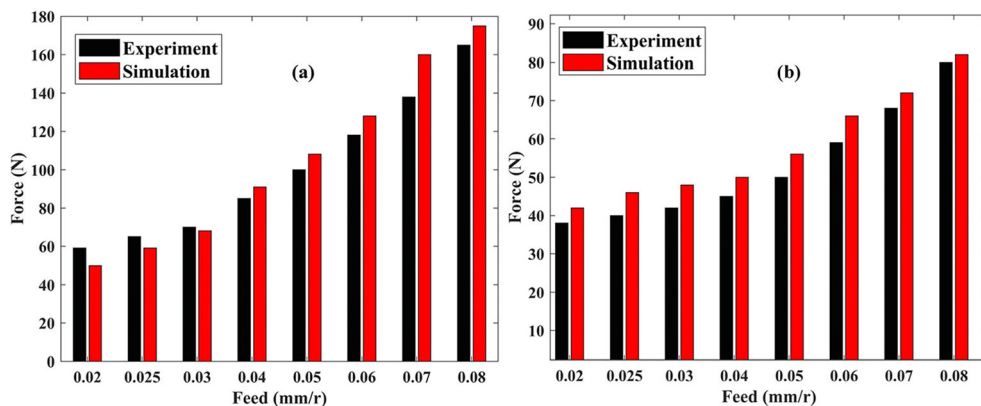


Fig. 9 Measurement of edge preparation using Alicona

Fig. 10 Comparison of simulation and experiment results. (a) Force in cutting direction. (b) Force in feed direction



precision instrument Alicona. The workpiece material used in the experiment is Al7075-T6, whose hardness is 150 HB. Cutting forces are measured by Kistler 9257B piezoelectric dynamometer and cutting data acquisition frequency is 50 Hz.

A series of tests have been implemented with various feeds, which is described as UCT in the orthogonal cutting. Besides, the cutting speed is 1600 mm/s and cutting width is 2 mm, which is the same with simulation setup. The comparison between experiment and simulation is shown in Fig.10. The predicted forces show in the same trend with the measured ones in both cutting and feed direction. The maximum, minimum errors of force in cutting direction are 14.8% and 3.8%, respectively. The maximum, minimum errors of force in feed direction are 19.1% and 2.0%, respectively.

5 Results and analysis

Section 2 details the complete process of implementing the method identifying three contact face components. In this

section, the results are shown and extended, including determining cutting mechanisms with various uncut chip thickness, identifying edge force components and exploring size effect phenomenon.

5.1 Chip formation

In cutting operation with rounded edge tool, chip formation with different feed is always an attractive issue worth exploring. Fang [30] researched the influence edge radius on chip formation in detail through slip line modeling. In this study, proposed contact forces can effectively reflect the chip formation under different uncut chip thickness.

Figure 11 researched three contact force components with various UCT. To make analysis more obvious, the figure is divided into three ranges with UCT increasing.

In range 1 (UCT is lower than h_s), only F_m exists and increases as enlarging UCT, meaning that contact behavior only happens in region m. Workpiece material is compressed into the surface by rounded edge without chip formation, which is

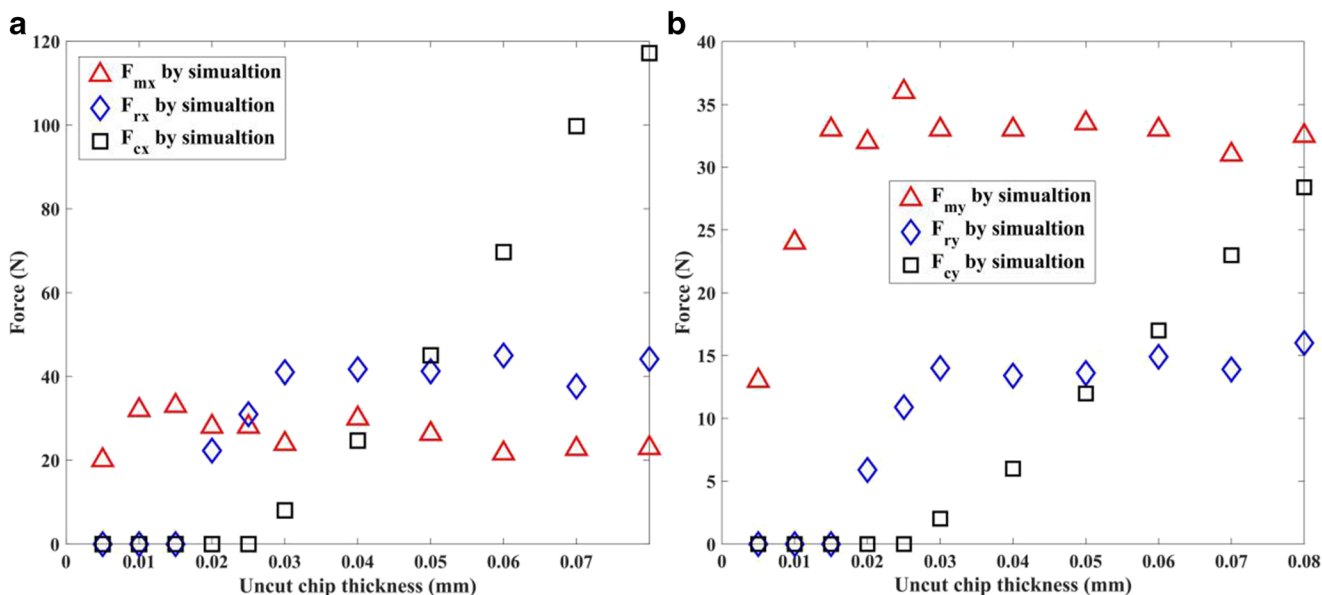
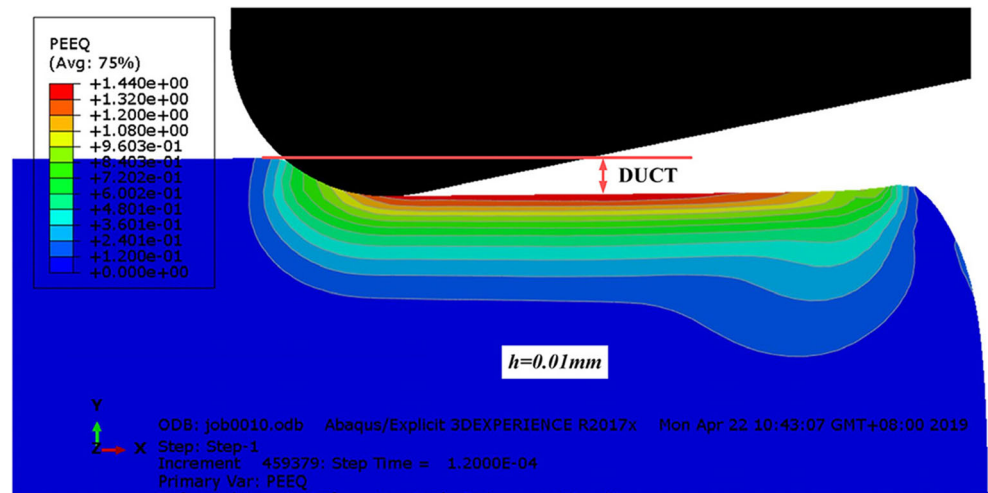


Fig. 11 Force components achieved by simulation. (a) Force components in cutting direction. (b) Force components in feed direction ($r_\beta = 0.039$ mm)

Fig. 12 Material deformation in range 1



illustrated in Fig. 12 in connection with the simulation result. All that occur is the elastic and plastic deformation of workpiece surface without material damage. It should be noted dynamic uncut chip thickness (DUCT) shown in Fig. 12 is similar to UCT in this situation ($h = 0.015$ mm).

With UCT continuing to increase, it comes to range 2 (UCT increases from 0.015 to 0.025 mm), F_m keeps constant and F_r increases. F_c is still zero, which means there is no interaction happening in region c. The attention should be paid to chip formation shown in Fig. 13(a), distinguished with traditional cutting situation with completely sharp tool, chip flows meanly along the round edge and the effective rake angle is strongly negative, affecting the calculations of cutting forces and temperature. However, when it comes to range 3 as shown in Fig. 13(b), the effective rake angle is not negative and chip appears both in region r and region c. In this range, F_r keeps stable and F_c increases from zero. Moreover, effective angle in region r is in a state of change with UCT increasing; thus, it is difficult and unreasonable to predict F_r with empirical shear model. As

shown in Fig. 11, F_r is predicted through FEM in this study, which is more simple and believable.

5.2 Elastic recovery

Figure 14 compares cutting forces in orthogonal cutting tests and cutting forces obtained by FEM in range 1. It can be seen that forces are underestimated both in cutting and feed direction by simulation. This mismatch can be explained by the elastic recovery theory. Elastic recovery phenomenon has been signified increasing the magnitude of cutting forces, especially in lower feed [31]. Figure 15 shows the elastic recovery in orthogonal cutting. If f is lower than the separation line, the surface material cannot be separated from workpiece and meanwhile elastic recovery happens with thickness of e_1 . As a result, when the cutting tool interacts with the machined surface in second time, the momentary feed increases to f_i calculated in Eq. (9). Moreover, f_i may be

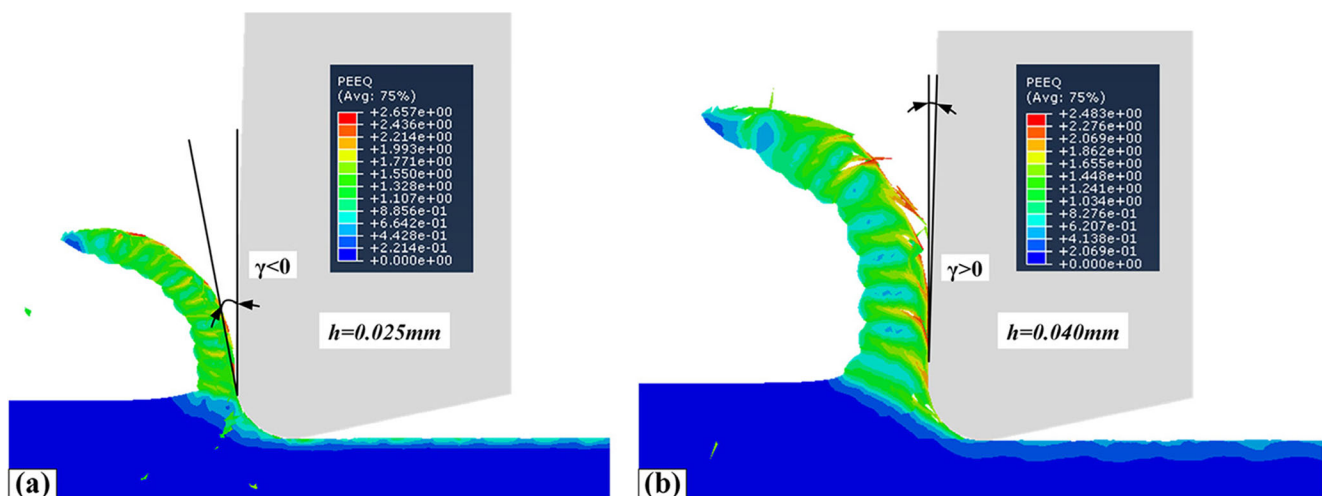


Fig. 13 Chip formation by FEM. (a) Chip formation in range 2. (b) Chip formation in range 3

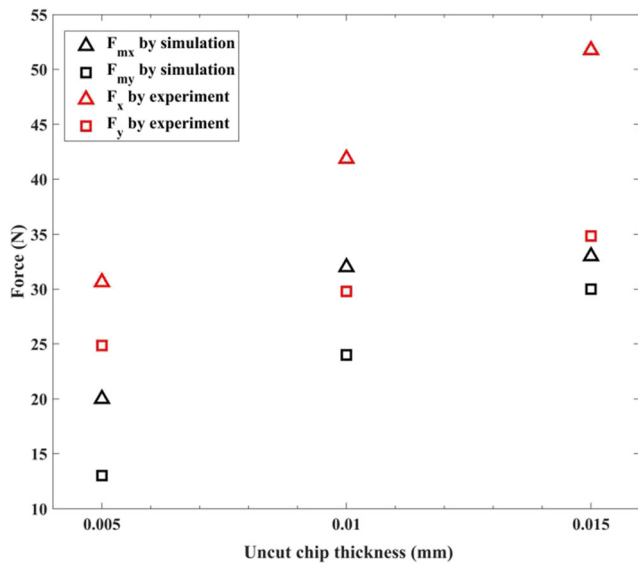


Fig. 14 Comparison between F and F_m in range 1

higher than the separation line, causing the chip formation with feed lower than 0.015 mm/r in orthogonal cutting tests.

$$f_t = f + e_1 \tag{9}$$

Therefore, it is the mismatch between UCT and feed caused by the elastic recovery that not only leads to a mismatch in cutting forces but also to the difference in chip formation with lower feed. Besides, elastic recovery also causes interaction between clearance face and machined surface. In the numerical orthogonal cutting model, interaction situation along clearance face is neglected and thus the simulated cutting forces are misestimated compared with experimental forces.

5.3 Edge force component

The edge force is defined as independent with UCT in semi-empirical cutting force model. However, as explored in Fig. 11, F_m keeps constant only when UCT is larger

Fig. 15 Elastic recovery in schematic diagram

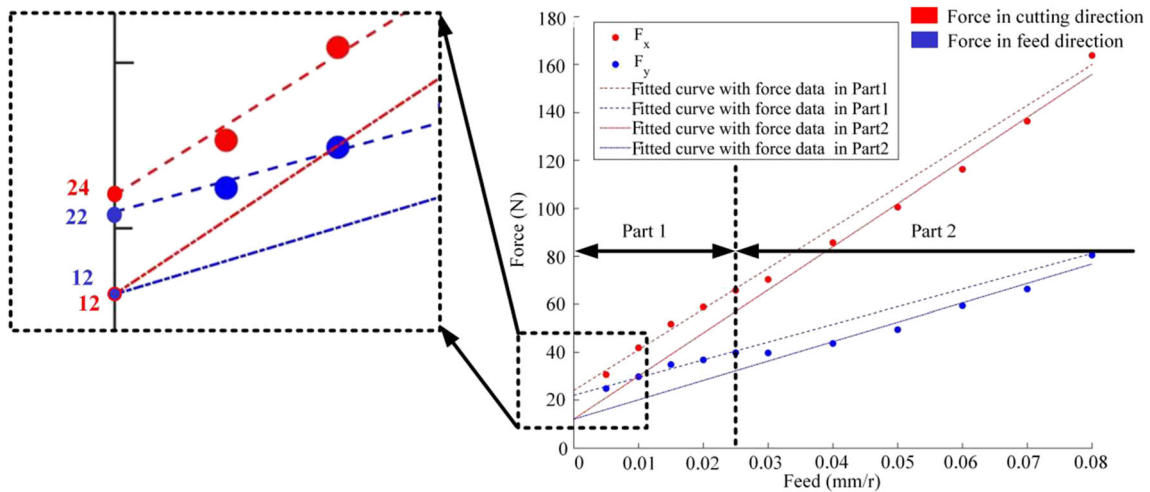
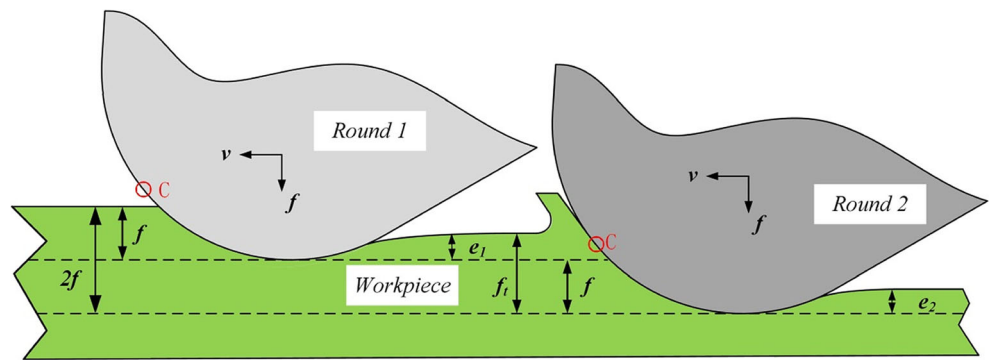


Fig. 16 Edge force values achieved by extrapolation way with experiment force data. Part 1: feed ranges from 0 to 0.025 mm/r. Part 2: feed ranges from 0.025 to 0.08 mm/r

than 0.015 mm. Thus, the value of F_m with $UCT = 0.015$ mm can be regarded as the value of edge force in semi-empirical cutting force model without considering interaction in clearance face.

Chip formation appears with feed lower than 0.015 mm/r in orthogonal cutting tests mainly for elastic recovery effect; thus, cutting force achieved at 0.015 mm/r in the experiment should not be regarded as the edge force. Methods of subtracting edge force component from total force have been being an attractive topic and extrapolation way, which regards edge force as the force with ideal zero feed, has been used popularly [12]. Extrapolation way is based on the assumption that the linear increase of total cutting forces is associated with increasing feed. However, the rate at which the cutting force increases with UCT is not constantly shown from Fig. 11. Combined with Fig. 13, it is the different effective rake angle which makes increasing rate different in different range. Effective rake angle is negative and changing with feed lower than 0.025 mm/r. When feed is larger than 0.025 mm/r, the effective rake angle keeps constant. In this theoretical basis, Fig. 16 is divided into two parts and cutting force is linearly fitted in two parts individually. Then all fitted curves are reversely prolonged to zero feed respectively and the value of edge force is achieved. Table 5 compares the value of edge force with extrapolation and simulation way. As a result, the error between simulation and extrapolation of the fitted curve 1 is relatively small. Therefore, it is more reasonable to use the forces in part 1 for extrapolation way in cutting process with round edge tool.

5.4 Size effect

Equation (10) defines the specific cutting energy in orthogonal cutting. Specific cutting energy is calculated as the ratio of total cutting force to the product of workpiece width and uncut chip thickness. Figure 17 shows the specific cutting energy with different UCT; K_x is specific cutting energy of cutting force. It increases nonlinearly with the decrease of UCT, which is defined as the size effect phenomenon. Moreover,

Table 5 The values of edge forces by simulation and extrapolation way

Edge forces (N)	Forces in cutting direction (N)	Forces in cutting direction (N)
Simulation	27	30
Curve in Part 1	24	22
Error 1	11%	27%
Curve in Part 2	12	12
Error 2	56%	60%

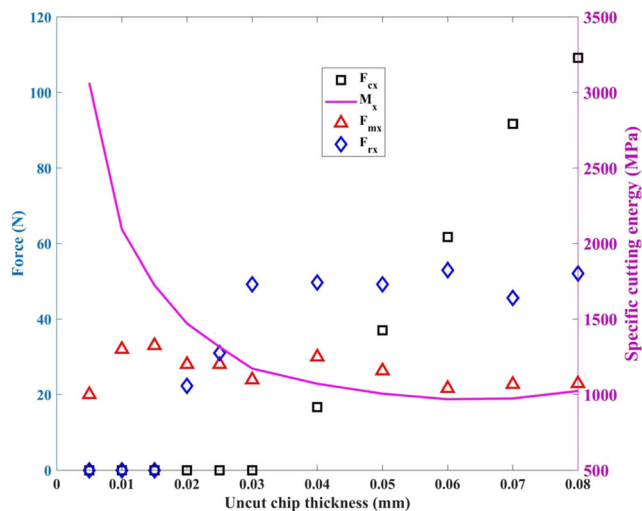


Fig. 17 Size effect of cutting direction in orthogonal cutting

the nonlinear increase mainly happens in range 1, where the plough mechanism is dominant. Some other researchers also thought size effect results from plough mechanism [10].

$$K_i = F_i/bh \quad (i = x, y) \tag{10}$$

Figure 18 explores specific cutting energy in cutting direction of contact force components, K_{mx} , K_{rx} and K_{cx} are specific cutting energy of three force components proposed, respectively. It shows K_{mx} decreases nonlinearly with UCT increasing. K_{rx} firstly increases and then gets maximum value from UCT which is 0.03 mm. After that, it decreases nonlinearly with UCT increasing. As for K_{cx} , it keeps up with UCT larger than 0.025 mm/r. Therefore, only K_{mx} exhibits size effect among UCT of all sizes, which proves the decisive effect of plough mechanism on size effect.

Besides, some researchers presented the cutter edge radius played and important role in size effect [32–34]. In this study,

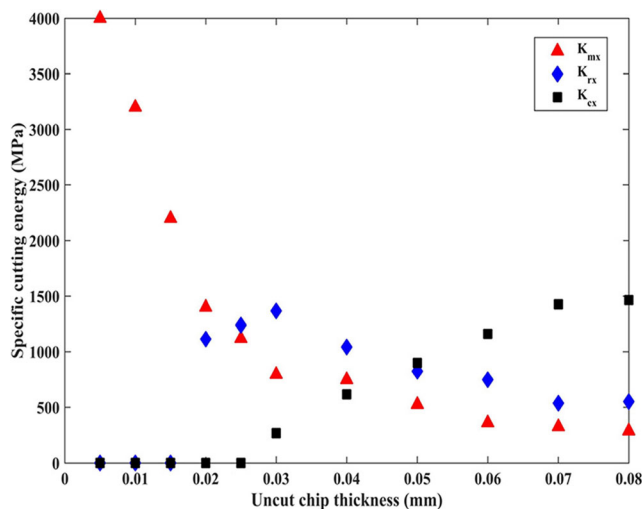


Fig. 18 Size effect of cutting direction in orthogonal cutting

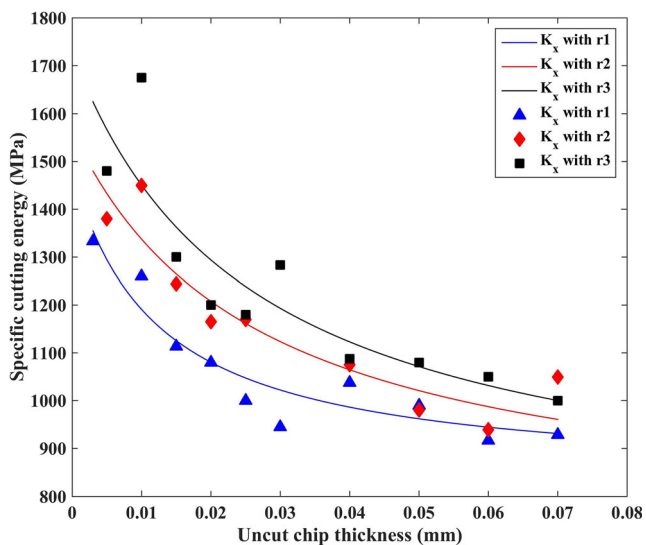


Fig. 19 Specific cutting energy with different rounded edge radius

a series of simulation tests are demonstrated to explore the relationship between size effect and round edge radius. Figure 19 shows the size effect with different round edge radius. UCT ranges from 0.005 to 0.07 mm and R_e increases from 0.01 to 0.03 mm. It offers obviously that the nonlinear increase of specific cutting energy reduces with decreased R_e . ($r_1 = 0.01$ mm, $r_2 = 0.02$ mm, $r_3 = 0.03$ mm)

6 Conclusions

In this paper, the generation of cutting forces is explored based on contact region identification in cutting with rounded edge tool. The separation line existing during plough process determines contact behavior between round edge and workpiece. The contribution of this paper can be given as follows:

1. A complicated and combined simulation method through FEM is developed to obtain three contact force components individually. Firstly, material separation is verified through nodal displacement in numerical simulation. Secondly, the numerical cutting model identifying three contact force components is established by partition function. Finally, all force values are detected and the whole cutting force can be achieved.
2. In orthogonal cutting, chip formation is affected by the radius of uncut chip thickness to edge radius. There is no chip formation with uncut chip thickness lower than 0.015 mm which can be considered as the minimum uncut chip thickness in this cutting situation. The interaction between chip and rake face occurs only when uncut chip thickness is larger than 0.025 mm.
3. Size effect is explored with the influence of round edge radius under various uncut chip thickness selections. The

result shows that size effect phenomenon is more obvious with larger edge radius.

Cutting forces achieved through FEM is in accordance with the orthogonal experiment results. The mismatch in low feed is believed to be caused by elastic recovery resulted from plough mechanism. The combination method between numerical simulation and analytical modeling will be explored to define elastic recovery behavior in cutting with rounded edge tool.

Funding information This work is partially supported by the National Natural Science Foundation of China (51705385, 51975237) and The Fundamental Research Funds for the Central Universities (2019-YB-019).

References

1. Weng J, Zhuang K, Zhu D, Guo S, Ding H (2018) An analytical model for the prediction of force distribution of round insert considering edge effect and size effect. *Int J Mech Sci* 138–139:86–98
2. Jiang L, Wang D (2019) Finite-element-analysis of the effect of different wiper tool edge geometries during the hard turning of AISI 4340 steel. *Simul Model Pract Theory* 94:250–263
3. Waldorf DJ, DeVor RE, Kapoor SG (1998) A slip-line field for ploughing during orthogonal cutting. *J Manuf Sci Eng* 120:693–699
4. Albrecht P (1960) New developments in the theory of the metal-cutting process: part I. The ploughing process in metal cutting. *J Eng Ind* 82:348–357
5. Basuray PK, Misra BK, Lal GK (1977) Transition from ploughing to cutting during machining with blunt tools. *Wear* 43:341–349
6. Liu Z (2013) Definition and determination of the minimum uncut chip thickness of microcutting. *Int J Adv Manuf Technol* 69:1219–1232
7. Yuan ZJ, Zhou M, Dong S (1996) Effect of diamond tool sharpness on minimum cutting thickness and cutting surface integrity in ultraprecision machining. *J Mater Process Technol* 62:327–330
8. Câmara MA, Abrão AM, Rubio JCC, Godoy GCD, Cordeiro BS (2016) Determination of the critical undeformed chip thickness in micromilling by means of the acoustic emission signal. *Precis Eng* 46:377–382
9. Wan M, Wen D-Y, Ma Y-C, Zhang W-H (2019) On material separation and cutting force prediction in micro milling through involving the effect of dead metal zone. *Int J Mach Tools Manuf* 146:103452
10. Aramcharoen A, Mativenga PT (2009) Size effect and tool geometry in micromilling of tool steel. *Precis Eng* 33:402–407
11. Arsecularatne JA (1997) On tool-chip interface stress distributions, ploughing force and size effect in machining. *Int J Mach Tool Manu* 37(7):885–899
12. Guo YB, Chou YK (2004) The determination of ploughing force and its influence on material properties in metal cutting. *J Mater Process Technol* 148:368–375
13. Wyen CF, Wegener K (2010) Influence of cutting edge radius on cutting forces in machining titanium. *CIRP Ann* 59:93–96
14. Armarego EJA, Whitfield RC (1985) Computer based modelling of popular machining operations for force and power prediction. *CIRP Ann Manuf Technol* 34:65–69
15. Stevenson R (1998) The measurement of parasitic forces in orthogonal cutting. *Int J Mach Tool Manu* 38:113–130

16. Weng J, Zhuang K, Hu C, Ding H (2020) A PSO-based semi-analytical force prediction model for chamfered carbide tools considering different material flow state caused by edge geometry. *Int J Mech Sci* 169:105329
17. Popov A, Dugin A (2013) A comparison of experimental estimation methods of the ploughing force in orthogonal cutting. *Int J Mach Tools Manuf* 65:37–40
18. Gonzalo O, Jauregi H, Uriarte LG, Lacalle LNL (2009) Prediction of specific force coefficients from a FEM cutting model. *Int J Adv Manuf Technol* 43:348–356
19. Jin X, Altintas Y (2012) Prediction of micro-milling forces with finite element method. *J Mater Process Technol* 212:542–552
20. Gao Q, Chen X (2019) Experimental research on micro-milling force of a single-crystal nickel-based superalloy. *Int J Adv Manuf Technol* 102:595–604
21. Wan L, Wang D (2015) Numerical analysis of the formation of the dead metal zone with different tools in orthogonal cutting. *Simul Model Pract Theory* 56:1–15
22. Woon KS, Rahman M, Neo KS, Liu K (2008) The effect of tool edge radius on the contact phenomenon of tool-based micromachining. *Int J Mach Tools Manuf* 48:1395–1407
23. Ulutan D, Özel T (2013) Determination of tool friction in presence of flank wear and stress distribution based validation using finite element simulations in machining of titanium and nickel based alloys. *J Mater Process Technol* 213:2217–2237
24. Vogler MP, Devor RE, Kapoor SG (2004) On the modeling and analysis of machining performance in micro-endmilling, part I: surface generation. *J Manuf Sci Eng* 126:685–694
25. Guo YB, Anurag S, Jawahir IS (2009) A novel hybrid predictive model and validation of unique hook-shaped residual stress profiles in hard turning. *CIRP Ann Manuf Technol* 58:81–84
26. Johnson GR, Cook WH (1983) A constitutive model and data for metals subjected to large strains, high strain rates and high temperatures. In: *Proceedings of the Seventh International Symposium on Ballistics*, Hague, The Netherlands 1983: 541–547
27. Brar NS, Joshi VS, Harris BW (2009) Constitutive model constants for AL7075T651 and AL7075T6. In: *American Institute of Physics Conference Series*, pp 945–948
28. Wang F, Qi T, Xiao L, Hu J, Xu L (2018) Simulation and analysis of serrated chip formation in cutting process of hardened steel considering ploughing-effect. *J Mech Sci Technol* 32(5):2029–2037
29. Giasin K, Ayvar-Soberanis S, French T, Phadnis V (2017) 3D finite element modelling of cutting forces in drilling fibre metal laminates and experimental hole quality analysis. *Appl Compos Mater* 24: 113–137
30. Fang N (2003) Slip-line modeling of machining with a rounded-edge tool—part II: analysis of the size effect and the shear strain-rate. *J Mech Phys Solids* 51:743–762
31. Liu X, Jun MBG, DeVor RE, Kapoor SG (2004) Cutting mechanisms and their influence on dynamic forces, vibrations and stability in micro-endmilling. *Proceedings of IMECE*, Anaheim, CA IMECE2004-62416, 2004: 583–592
32. Özel T (2009) Modelling and simulation of micro-milling process. *Mater Manuf Process* 24:21–23
33. Liu X, DeVor RE, Kapoor SG, Ehmann KF (2005) The mechanics of machining at the microscale: assessment of the current state of the science. *J Manuf Sci Eng* 126:666–678
34. Liu K, Melkote SN (2007) Finite element analysis of the influence of tool edge radius on size effect in orthogonal micro-cutting process. *Int J Mech Sci* 49:650–660

Publisher's note Springer Nature remains neutral with regard to jurisdictional claims in published maps and institutional affiliations.